Thermally driven convection in Li||Bi liquid metal batteries

Personnettaz, P.; Beckstein, P.; Landgraf, S.; Köllner, T.; Nimtz, M.; Weber, N.; Weier, T.;

Publiziert:

September 2018

Journal of Power Sources 401(2018), 362-374

DOI: https://doi.org/10.1016/j.jpowsour.2018.08.069

Thermally driven convection in Li||Bi liquid metal batteries

Paolo Personnettaz[a,b], Pascal Beckstein[a], Steffen Landgraf[a], Thomas Köllner[a,c], Michael Nimtz[a], Norbert Weber[a], Tom Weier[a]

[a] *Helmholtz-Zentrum Dresden – Rossendorf, Bautzner Landstr. 400, 01328 Dresden, Germany*
[b] *Politecnico di Torino, Corso Duca degli Abruzzi 24, 10129 Torino, Italy*
[c] *University of California, Santa Barbara, CA 93106, USA*

Abstract

Liquid Metal Batteries (LMBs) are a promising concept for cheap electrical energy storage at grid level. These are built as a stable density stratification of three liquid layers, with two liquid metals separated by a molten salt. In order to ensure a safe and efficient operation, the understanding of transport phenomena in LMBs is essential. With this motivation we study thermal convection induced by internal heat generation. We consider the electrochemical nature of the cell in order to define the heat balance and the operating parameters. Moreover we develop a simple 1D heat conduction model as well as a fully 3D thermo-fluid dynamics model. The latter is implemented in the CFD library OpenFOAM, extending the volume of fluid solver, and validated against a pseudo-spectral code. Both models are used to study a rectangular 10×10 cm Li||Bi LMB cell at three different states of charge.

Keywords: liquid metal batteries, heat transfer, thermal convection, thermodynamics, OpenFOAM, volume of fluid, spurious currents

1. Introduction

Grid-level storage will be an indispensable ingredient of future energy systems dominated by volatile renewable electricity sources [1]. As of today, storage options are limited and far from available in the required capacity [2]. Liquid metal batteries (LMBs) might help to economically bridge the storage gap [3].

An LMB consists of a low-density liquid metal negative electrode, an intermediate-density molten salt electrolyte, and a high-density liquid metal positive electrode (Fig. 1) [4]. As the name indicates, the operating temperature is such that each phase is in a liquid state. Typical negative electrode materials are K, Li, Na [5–7] and more recently Ca [8] and Mg [4]. Positive electrodes can consist of Bi, Pb, Sn [6], Hg [5], Se, Te [7], as well as Sb [4] and other metals. From the perspective of fluid dynamics, LMBs are multi-physics systems that couple electrochemical reactions, thermal effects, mass transport, electric currents, magnetic fields, and phase changes with fluid flow. In the last years, several studies have been dedicated to model time and space resolved physical processes in LMBs, for a recent review see [9]. These studies were aimed at uncovering the non-equilibrium processes during operation as well as at addressing crucial design problems. A central issue has been the mechanical integrity of the electrolyte layer. Its height is governed by conflicting objectives, i.e., the reduction of ohmic losses (thin electrolyte) versus safety against short circuits (thick electrolyte).

Fluid-dynamical research has focused so far mainly on 'differential density cells' containing three liquid layers in stable stratification but free to move (Fig. 1, center). Electrochemical cell characteristics are often reported

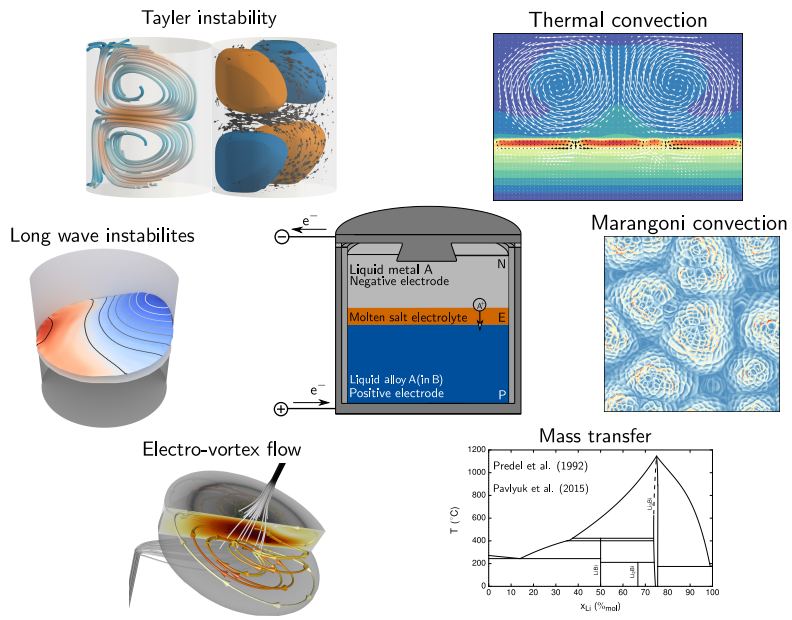

Figure 1: Sketch of an LMB with typical inventory (middle) and expected fluid dynamics and transport phenomena in LMBs.

for configurations featuring a retainer for the negative electrode, typically a metal foam, e.g., [10].

Several studies have shown that fluid motion can be triggered by magneto-hydrodynamic effects, i.e., the interaction of a magnetic field (either a background field or the field caused by the battery current) with the cell current. This includes the Tayler instability [11–16], electro-vortex flows [17–21] as well as interface instabilities [22–27]. While the Tayler instability will get substantial only for large system (in the order of meters) [14], electro-vortex flow will appear already in small cells [19]. Long wave interface instabilities may endanger the safe operation of medium to large size LMBs [24, 26].

For laboratory scale experiments, thermal convection is an important

source of fluid motion. Temperature gradients (producing forces by density and interfacial-tension gradients) seem to be unavoidable due to either heating or cooling from the surroundings. In this context, Wang et al. [28] studied pure heat conduction in a single cell. Kelley et al. [29, 30] experimentally showed how buoyant convection can be enhanced by applying a current to a liquid-metal electrode heated from below [31]. Shen and Zikanov [32] studied numerically the buoyant convection driven by ohmic heating in a three-layer liquid metal battery with plane, horizontal interfaces. This work suggests that heating always triggers convection in the electrolyte layer for practical configurations. Shen and Zikanov [32] further found the influence of the discharge current's magnetic field on thermal convention to be negligible for laboratory scales. Köllner et al. [33] extended the work of Shen and Zikanov [32] by taking into account the temperature dependency of the interfacial tensions and the different transport coefficients of the layers. Choosing a typical material combination of Li separated by LiCl−KCl from Pb−Bi, Köllner et al. [33] first analyzed the linear stability of the stationary pure conduction state. Furthermore, they performed three-dimensional direct-numerical simulations using a pseudo-spectral method while varying electrolyte layer heights, cell heights, and current densities. Four instability mechanisms were identified: 1) buoyant convection in the upper electrode, 2) buoyant convection in the molten salt layer, and 3,4) Marangoni convection at both interfaces between molten salt and electrode. The instability mechanisms are partly coupled to each other. Köllner et al. [33] could confirm the Shen and Zikanov's [32] conclusion that buoyant convection in the salt layer is the most critical one. However, this convection might be sup-

pressed for small layer heights and low current densities. The Marangoni effect was found to support buoyant convection as long as the electrolyte layer thickness remains below one tenth of the upper electrode height. For thicker Li electrodes, buoyant convection is most active in the upper layer causing interfacial stresses to counteract convection.

Recent progress notwithstanding, modeling of LMBs is far from being comprehensive. Temperature variations discussed so far in the literature were based only on a few selected terms of the actual internal energy balance as given, e.g., by [34]. One of the so far disregarded terms is the electrochemical heat, which can be estimated using equilibrium thermodynamics.

This heat contribution warms or cools the positive electrode whenever the ions of the negative electrode metal alloys or dealloys with the positive electrode material. A similar effect was found in simple ternary system of organic solvents with interfacial reactions [35]. Experiments that involved exothermic interfacial reaction revealed intriguing fluid motion [36].

The paper at hand will extend the previous work of Shen and Zikanov [32] and Köllner et al. [33] by 1) including the electrochemical heat, 2) allowing the interfaces to be deformable, 3) considering different states of charge, and 4) including the lateral walls. The article proceeds as follows: in section 2 we discuss the electrochemistry of the cell and we derive the electrochemical heat. Section 4 gives a discussion of possible thermal phenomena relevant for an LMB. We derive a model for the pure conduction state and we describe the simulation model. Finally, the results are discussed and summarized in a conclusion.

2. Thermodynamics and electrochemistry

The characterization and quantification of the heat sources during cell charge and discharge is later used in the modeling and simulation of the thermal processes in an LMB cell. This requires the study of the thermodynamic and electrochemical processes in such a cell.

The chosen chemistry in this study is Li||Bi, which was experimentally investigated from the electrochemical perspective by Ning et al. [10]. Furthermore, there is extensive literature (compared to other electrode pairs) on the thermodynamic properties of Bi−Li alloys [37–48], allowing for good estimations. The considered molten salt electrolyte is KCl−LiCl, with a near eutectic composition (41.5 $\%_{\mathrm{mol}}$ KCl). It is not stable in the cell environment [42], but it is the only one for which all material properties are available.

The cell type studied is a fully liquid binary concentration cell. In the positive electrode, during discharge, oxidized lithium ions and bismuth atoms form a fully liquid single phase alloy (Li (in Bi) or $\mathrm{Li}_{(\mathrm{Bi})}$) [10]. This condition is satisfied up to a certain molar fraction of lithium (liquidus line), $x_{\mathrm{liq}}(T) = 39.5\,\%_{\mathrm{mol}}$, at the temperature of interest $T = 450\,°\mathrm{C}$. For a higher concentration of lithium, the solid intermetallic phase $\mathrm{Li_3Bi}$ starts to be deposited [10]. This second region of operation is not investigated, due to the fact that the presence of a floating solid phase introduces further complexities from a thermodynamic and thermo-fluid dynamic point of view.

The cell is studied at three different molar fractions of lithium in bismuth x_{Li}, at 1, 10 and 38 $\%_{\mathrm{mol}}$ $\mathrm{Li}_{(\mathrm{Bi})}$.

2.1. Equilibrium cell quantities

The equilibrium cell voltage and the electrochemical heat are derived in this paragraph. Both quantities are needed later to compute the polarization curves, and to simulate thermal phenomena in the LMB.

The equilibrium cell voltages can be taken from the experimental results of electrochemical studies of Bi−Li alloys [42, 43, 46]. It is directly related to the variation of partial molar Gibbs free energy of Li in Bi $\Delta\overline{G}_{\mathrm{Li}}$ with respect to the pure Li state. The equilibrium cell voltage $E_{\mathrm{cell,eq}}$ is

$$E_{\mathrm{cell,eq}} = -\frac{\Delta\overline{G}_{\mathrm{Li}}}{n_{\mathrm{e^-}} \cdot \mathrm{F}} \ , \tag{1}$$

in which $n_{\mathrm{e^-}}$ is the number of electrons transferred per ion ($n_{\mathrm{e^-}} = 1$ for Li||Bi) and F is the Faraday constant [4].

The electrochemical heat $\dot{Q}_{\mathrm{r}}$ can be derived from the first and second principle of thermodynamics applied to the cell, assuming a uniform concentration of Li in the positive electrode and a complete interaction with the whole amount of Bi. These hypotheses are valid only in a 0D model. Nevertheless, they are used in the following derivation due to the absence of a mass transport model (describing the concentration distribution in the positive electrode). The electrochemical heat $\dot{Q}_{\mathrm{r}}$ as a function of the molar flow rate of Li $\dot{n}_{\mathrm{Li}}$ is

$$\dot{Q}_{\mathrm{r}} = \pm \underbrace{\frac{j \cdot A}{n_{\mathrm{e^-}} \cdot \mathrm{F}}}_{\dot{n}_{\mathrm{Li}}} (T\Delta\overline{S}_{\mathrm{Li}} + \frac{1 - x_{\mathrm{Li}}}{x_{\mathrm{Li}}} \Delta\overline{H}_{\mathrm{Bi}}) \ , \tag{2}$$

in which j denotes the absolute value of the current density, A the cross sectional area of the cell, x_{Li} the molar fraction of lithium in bismuth, $\Delta\overline{S}_{\mathrm{Li}}$ the partial molar entropy of Li and $\Delta\overline{H}_{\mathrm{Bi}}$ the partial molar enthalpy of bismuth. The plus sign in the formulation refers to discharge and the minus refers to

charge. Positive values refer to heat that is absorbed, i.e. the cell cools down. The electrochemical heat includes two terms. The first term is the classical isothermal reversible heat term $T\Delta\overline{S}_{\mathrm{Li}}$, directly related to the temperature coefficient of the cell equilibrium voltage $\frac{\mathrm{d}E_{\mathrm{cell,eq}}}{\mathrm{d}T}$ [49]. The second one is an additional term that takes into account the variation of enthalpy of bismuth. The bismuth atoms are not directly affected by the electrochemical reaction, but they mix with lithium atoms, so they contribute to the heat generation term with their enthalpy of mixing. The presence of this second term introduces non negligible differences, as Tab. 1 shows, but globally the electrochemical heat remains in the same order of magnitude as the reversible one.

If the electrochemical heat is divided by the molar flow rate of Li $\dot{n}_{\mathrm{Li}}$ (which is related to the electrical current through the Faraday law) it is possible to define the electrochemical heat $\overline{q}_{\mathrm{r,Li}}$ per unit mole of Li:

$$\overline{q}_{\mathrm{r,Li}} = \frac{\dot{Q}_{\mathrm{r}}}{\dot{n}_{\mathrm{Li}}} = \pm\Big(T\Delta\overline{S}_{\mathrm{Li}} + \frac{1-x_{\mathrm{Li}}}{x_{\mathrm{Li}}}\Delta\overline{H}_{\mathrm{Bi}}\Big) = \pm\frac{1}{x_{\mathrm{Li}}}(T\Delta\overline{S} + (1-x_{\mathrm{Li}})\Delta\overline{G}_{\mathrm{Bi}})\ , \quad (3)$$

in which $\Delta\overline{S}$ is the total entropy variation and $\Delta\overline{G}_{\mathrm{Bi}}$ is the partial molar Gibbs free energy of bismuth.

The thermoneutral voltage E_{TN} for LMBs is then defined as

$$E_{\mathrm{TN}} = -\frac{\Delta\overline{G}_{\mathrm{Li}}}{n_{\mathrm{e^-}}\cdot\mathrm{F}} - \frac{\overline{q}_{\mathrm{r,Li}}}{n_{\mathrm{e^-}}\cdot\mathrm{F}} = E_{\mathrm{cell,eq}} - \frac{\overline{q}_{\mathrm{r,Li}}}{n_{\mathrm{e^-}}\cdot\mathrm{F}}\ . \quad (4)$$

If the cell voltage E_{cell} is equal to the thermoneutral voltage, the heat generated by overpotentials (irreversibilities) is balanced by the electrochemical heat. This is true only in point-like (0D) isothermal cells.

The values of the thermodynamic quantities ($\Delta\overline{G}_{\mathrm{Li}}$, $\Delta\overline{G}_{\mathrm{Bi}}$, $\Delta\overline{H}_{\mathrm{Bi}}$, $\Delta\overline{S}$ and $\Delta\overline{S}_{\mathrm{Li}}$) and the equilibrium quantities ($E_{\mathrm{cell,eq}}$, $\overline{q}_{\mathrm{r,Li}}$, E_{TN}) are calculated from

the experimental results of Gasior et al. [46]. They measured the equilibrium cell voltage $E_{\mathrm{cell,eq}}$ and its temperature coefficient $\frac{\mathrm{d}E_{\mathrm{cell,eq}}}{\mathrm{d}T}$ for a wide range of concentrations and temperatures close to the region of interest. In order to avoid further approximations due to extrapolation, the thermodynamic values are evaluated at $T_{\mathrm{G}} = 775\,\mathrm{K}$ (the subscript G refers to Gasior et al.). For the same reason, the fully charged cell is studied with the values at $x_{\mathrm{Li}} = 1\,\%$. Numerical integration of the Gibbs-Duhem equation is used in order to define all quantities of interest. All values are collected in Tab. 1. The equilibrium cell voltage $E_{\mathrm{cell,eq}}$ and the thermoneutral voltage E_{TN} for the fully charged state are shown in Fig. 2 as black lines.

2.2. Polarization curve and parameters definition

The equilibrium cell potential $E_{\mathrm{cell,eq}}$, and the study of classical overpotential theory allow to estimate the polarization curve of Li||Bi LMBs. Knowing the polarization curve is crucial to define realistic electrolyte layer thicknesses and current densities.

The fully-liquid interfaces between electrolyte and electrodes guarantee very fast charge transfer kinetics [4, 50, 51], allowing to neglect the charge transfer overpotential. Furthermore, the fast diffusion in the liquid metal electrode ensures efficient mass transport during operation. For a first estimate it seems therefore reasonable to neglect the concentration overpotential [4, 50]. The ohmic overpotential is consequently the most relevant inefficiency of LMBs. The simplified polarization curve $E_{\mathrm{cell}}(j)$ is [52]:

$$E_{\mathrm{cell}}(j) = E_{\mathrm{cell,eq}} \pm \sum_i \eta_i(j) \cong E_{\mathrm{cell,eq}} \pm \rho_{\mathrm{el,E}} \cdot \Delta h_{\mathrm{E}} \cdot j \; = E_{\mathrm{cell,eq}} \pm \Delta E_{\mathrm{cell},\Omega} \; , \quad (5)$$

in which $\rho_{\mathrm{el,E}}$ is the electrical resistivity of the molten salt electrolyte and

Table 1: Thermodynamic properties and electrochemical heat for three different charge states of a Li||Bi cell. Data calculated from Gasior et al. at $T_{\mathrm{G}} = 775\,\mathrm{K}$ [46].

property	unit	cases studied		
x_{Li}	%	1	10	38
$E_{\mathrm{cell,eq}}$	V	1.05	0.88	0.73
$\frac{\mathrm{d}E_{\mathrm{cell,eq}}}{\mathrm{d}T}$	$\mu\mathrm{V\,K^{-1}}$	255	96	−47.6
$\Delta\overline{S}_{\mathrm{Li}}$	$\mathrm{J\,mol_{Li}^{-1}K^{-1}}$	24.6	9.3	−4.6
$\Delta\overline{H}_{\mathrm{Bi}}$	$\mathrm{kJ\,mol_{Bi}^{-1}}$	0	−0.19	−1.0
$T_{\mathrm{G}}\Delta\overline{S}_{\mathrm{Li}}$	$\mathrm{kJ\,mol_{Li}^{-1}}$	19	7.2	−3.6
$\Delta\overline{S}$	$\mathrm{J\,mol_{tot}^{-1}K^{-1}}$	0.33	1.83	2.24
$T_{\mathrm{G}}\Delta\overline{S}$	$\mathrm{kJ\,mol_{tot}^{-1}}$	0.25	1.4	1.7
$\Delta\overline{G}_{\mathrm{Bi}}$	$\mathrm{kJ\,mol_{Bi}^{-1}}$	−0.065	−0.78	−4.99
$\overline{q}_{\mathrm{r,Li}}$	$\mathrm{kJ\,mol_{Li}^{-1}}$	19	5.5	−5.2
E_{TN}	V	0.86	0.82	0.79

Δh_{E} is the thickness of this layer; plus refers to the charge of the cell, minus refers to the discharge. The resulting linear profile is shown quite clearly in the report of Chum et al. [53] for the case of a Li||Bi bimetallic cell.

It is important to notice that the simplifications mentioned above are not valid for all type of LMBs (e.g. Ca||Bi [8]) and operating conditions. For

example, if the composition of the alloy locally (at the interface) reaches the one of the liquidus line, an additional nucleation overpotential occurs. In order to unveil all these complexities, the mass transport and the electrochemical phenomena must be introduced inside the model.

The presented polarization model does not depend on the state of charge of the cell. It allows the direct connection of two important parameters: the thickness of the electrolyte Δh_{E} and the current density j through the ohmic overpotential of the cell $\Delta E_{\mathrm{cell},\Omega}$. This connection will be used later in the heat conduction model.

The estimated polarization curves $E_{\mathrm{cell}}(j)$, for charge and discharge, are shown in Fig. 2 as a function of the thickness Δh_E of the electrolyte layer. The thermoneutral voltage divides the polarization plot (in discharge mode, Fig. 2a) in two regions. In the upper region ($E_{\mathrm{cell}} > E_{\mathrm{TN}}$), the negative electrochemical heat (blue arrow) is predominant and the cell is globally cooled (adiabatic conditions assumed). In the lower region of the plot (in discharge mode, Fig. 2a) the heating due to the ohmic overpotential is the most important and the cell is globally heated. During charging (Fig. 2b) both effects (electrochemical and ohmic) heat up the cell (red arrows). These considerations are valid only for the chosen $x_{\mathrm{Li}} = 1\,\%$, they strictly depend on the sign of the electrochemical heat per unit mole of Li $\overline{q}_{\mathrm{r,Li}}$.

3. Cell geometry

We define a square-based cell with 100 mm side length L and denote the three phases from bottom to top as P (positive electrode), E (electrolyte) and N (negative electrode), as shown in Fig. 3. In the first case, the fully charged

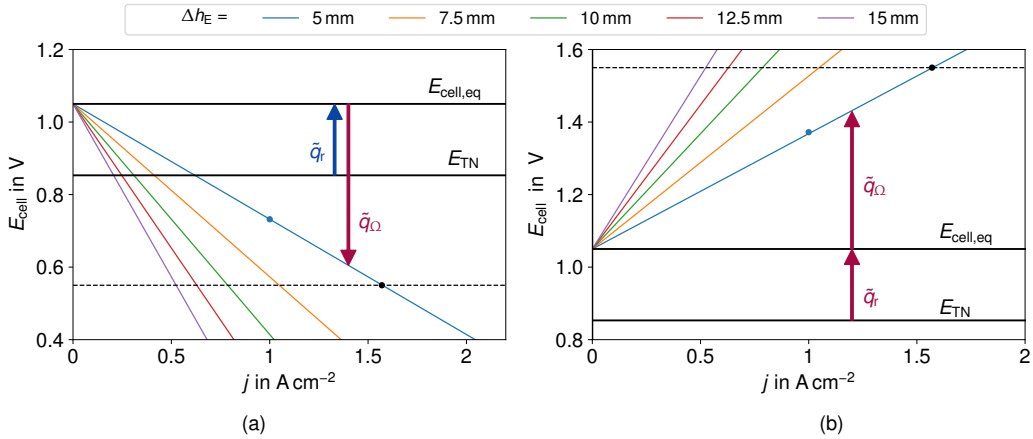

Figure 2: Polarization curve at $x_{\mathrm{Li}} = 1\,\%$ as function of the thickness of the electrolyte (Δh_{E}), for discharge (a) and charge (b) according to Eq. 5. The arrows are proportional to the heat generated (red) or absorbed (blue) per unit of current. The ohmic term ($\tilde{q}_{\Omega} = -\rho_{\mathrm{el,E}} \cdot j \cdot h_{\mathrm{E}}$) is proportional to current, while the electrochemical term ($\tilde{q}_{\mathrm{r}} = \pm \frac{\overline{q}_{\mathrm{r,Li}}}{n_{\mathrm{e^-}} \cdot \mathrm{F}}$) is constant. The blue dot marks the investigated condition with the fully 3D simulation. The dashed line refers to the assumed maximum voltage drop of $\Delta E_{\mathrm{cell},\Omega} = 0.5\,\mathrm{V}$. The black dot marks the maximum current density used in this study.

cell is studied. The height of the liquid bismuth layer is $\Delta h_{\mathrm{P}} = 20\,\mathrm{mm}$; the electrolyte thickness is $\Delta h_{\mathrm{E}} = 5\,\mathrm{mm}$. The maximum possible discharge capacity of Li||Bi is given by the maximum molar fraction of lithium in the positive electrode, namely $x_{\mathrm{Li}} = 75\,\%$ [10]. This results in a height of the lithium layer of about $\Delta h_{\mathrm{N}} = 40\,\mathrm{mm}$. For the partly discharged cells ($x_{\mathrm{Li}} = 10\,\%, 38\,\%$), the thickness of the liquid metal layers vary due to the amount of lithium transferred and the different densities of the alloys. These data are collected in Tab. C.3. The values of the material properties of the components and their derivation are collected in Appendix C.

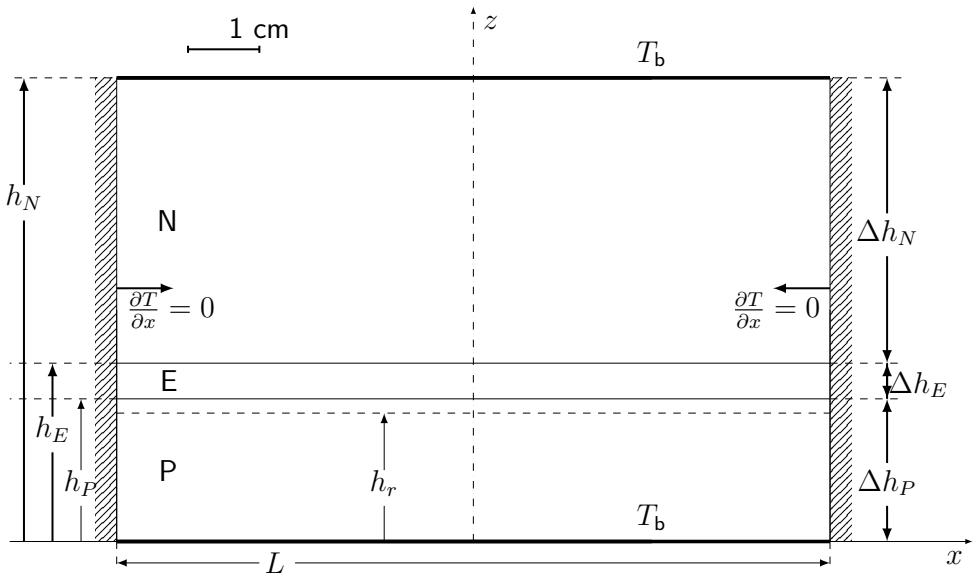

Figure 3: Cell dimensions and thermal boundary conditions.

4. Thermal modeling

4.1. Thermal phenomena and main assumptions

The temperature field in a liquid metal battery may change due to several internal heat generation phenomena [34, 49]:

- Joule heating induced by overpotentials
- chemical and electrochemical reactions
- phase changes

Furthermore, heat is transferred by conduction, advection and radiation as well as the Dufour effect (i.e. transport due to compositional gradients). Note that mass transport and the chemical reactions induce composition variations that may influence the thermodynamics (heat of mixing) and material properties, but which are out of the current scope. Finally, the cell is a

closed system that thermally interacts with the environment and the thermal management system [54]. In order to manage properly this problem with the available data, several assumptions will be made.

Ohmic heating of the electrolyte is usually the most important overpotential in an LMB, as demonstrated in paragraph 2.2. However, the electrochemical heat released when alloying Li into Bi may become important especially at low charge or discharge currents [4]. We include (only) these two heat sources in our models and neglect solidification. A uniform current distribution is assumed, ignoring MHD effects. The composition of each layer is assumed to be constant and homogeneous.

Regarding the interaction with the external environment, we assume a simplified configuration similar to the one employed in previous studies [32]. Only the three liquid layers are studied; the heat transfer in the gas layer and in the cell containment is neglected as well as radiative heat transfer (in the salt and argon layer). The lateral walls are assumed adiabatic, whereas the bottom and the top are considered isothermal at $T_\mathrm{b} = 450\,°\mathrm{C}$, as shown in Fig. 3. The cell is investigated in thermal steady state condition.

4.2. One-dimensional heat conduction model

In this paragraph we study pure conduction only, because it allows an analytical treatment. It provides a good approximation for small fluid velocities and likewise an upper bound for the cell temperature. For pure conduction and in a steady state limit, the temperature field depends only on the vertical coordinate z as [55]

$$-k_i \frac{\mathrm{d}^2 T}{\mathrm{d}z^2} = \dot{q}_i''' \tag{6}$$

with z denoting the vertical coordinate and T the temperature; k_i and $\dot{q}_i'''$ are the thermal conductivity and the heat generation term of layer i. These three ordinary differential equations are coupled with appropriate interface conditions: the continuity of temperature and heat flux are enforced. We neglect Joule heating in the metal layers because of their low electrical resistivity.

The electrochemical heat source is modeled in two different ways: as a volumetric and interfacial effect. Both approaches have been already employed for the study of the thermal behavior of batteries [34, 56–58], since an exact treatment would require a complicated mass transfer model. In the volumetric approach, the positive electrode is split into two parts. The electrochemical heat is generated only in the active layer of height $\Delta h_\mathrm{r} = h_\mathrm{P} - h_\mathrm{r}$, and a homogeneous equation is solved in the inactive layer. The volumetric heat generation reads:

$$\dot{q}_i''' = \begin{cases} 0 & \text{for } 0 < z < h_\mathrm{r} \quad \text{inactive positive electrode} \\ \dot{q}_\mathrm{r}''' = -\dfrac{j\overline{q}_\mathrm{r,Li}}{n_\mathrm{e\text{-}}\mathrm{F}\Delta h_\mathrm{r}} & \text{for } h_\mathrm{r} < z < h_\mathrm{P} \quad \text{active positive electrode} \\ \dot{q}_{\Omega,\mathrm{E}}''' = \rho_\mathrm{el,E} j^2 & \text{for } h_\mathrm{P} < z < h_\mathrm{E} \quad \text{electrolyte} \\ 0 & \text{for } h_\mathrm{E} < z < h_\mathrm{N} \quad \text{negative electrode .} \end{cases} \tag{7}$$

In the interfacial model, the electrochemical heat generation is imposed on the interface between the positive electrode and the electrolyte ($z = h_\mathrm{P}$) as a discontinuity of the heat flux (this approximation is also employed for Peltier heat [59]):

$$-k_\mathrm{E}\frac{\mathrm{d}T}{\mathrm{d}z}\Big|_{z=h_\mathrm{P}+\epsilon} + k_\mathrm{P}\frac{\mathrm{d}T}{\mathrm{d}z}\Big|_{z=h_\mathrm{P}-\epsilon} = \underbrace{-\frac{j\overline{q}_\mathrm{r,Li}}{n_\mathrm{e\text{-}}\mathrm{F}}}_{\dot{q}_\mathrm{r}''} , \tag{8}$$

with ϵ denoting an infinitesimal distance. The solution of the general formu-

lation that takes into account both electrochemical heat generation models is expressed by the following temperature distribution:

$$T = \begin{cases} c_1 \cdot z + c_2 & \text{for } 0 < z < h_0 \quad \text{inactive positive electrode} \\ -\dfrac{\dot{q}_{\mathrm{r}}'''}{2k_{\mathrm{P}}} \cdot z^2 + c_3 z + c_4 & \text{for } h_0 < z < h_{\mathrm{P}} \quad \text{active positive electrode} \\ -\dfrac{\dot{q}_{\Omega,\mathrm{E}}'''}{2k_{\mathrm{E}}} \cdot z^2 + c_5 z + c_6 & \text{for } h_{\mathrm{P}} < z < h_{\mathrm{E}} \quad \text{electrolyte} \\ c_7 \cdot z + c_8 & \text{for } h_{\mathrm{E}} < z < h_{\mathrm{N}} \quad \text{negative electrode} \end{cases} \tag{9}$$

with the parameters c_i given in Appendix B, where it is understood that either $\dot{q}_{\mathrm{r}}'''$ or $\dot{q}_{\mathrm{r}}''$ vanishes. The maximum cell temperature $T_{\max}$ and its position $z_{\max}$ are

$$T_{\max} = \frac{k_{\mathrm{E}} c_5^2}{2\dot{q}_{\Omega}'''} + c_6 \quad \text{at} \quad z_{\max} = \frac{k_{\mathrm{E}} c_5}{\dot{q}_{\Omega}'''} \ , \tag{10}$$

with the maximum value being a parabolic function of the current density. In Fig. 4 we present some results derived from the analytical model. Fig. 4a shows the maximum temperature difference in the cell for typical current densities and electrolyte thicknesses during discharge, and without electrochemical heat generation. Assuming a fixed ohmic drop $\Delta E_{\mathrm{cell},\Omega}$, it is possible to relate the current density to the thickness of the electrolyte by applying Eq. 5. This allows to bound the current and electrolyte thickness to an admissible region. If the ratio between the thickness of the layers is fixed (Fig. 4a with $\Delta h_{\mathrm{P}}/\Delta h_{\mathrm{E}} = 4$ and $\Delta h_{\mathrm{N}}/\Delta h_{\mathrm{P}} = 2$), the curves for constant $\Delta T_{\max}$ and constant $\Delta E_{\mathrm{cell},\Omega}$ coincide.

Starting from these consideration it is possible to derive the results presented in Fig. 4b. It shows the maximum temperature difference as a function of the ohmic overpotential and the ratio $\Delta h_{\mathrm{P}}/\Delta h_{\mathrm{E}}$, at fixed $\Delta h_{\mathrm{N}}/\Delta h_{\mathrm{P}} = 2$.

The temperature rises up in the cell due to the increase of the ohmic voltage drop and due to the increase of the thickness of the liquid metal layers.

Fig. 4c shows the vertical temperature profile in the fully charged cell at the maximum current density ($j_{\max} = 1.57\,\mathrm{A\,cm^{-2}}$). Positive (red), negative (blue) and null (green) electrochemical heat generation are presented. The temperature profiles in the top electrode and in the electrolyte are always linear and parabolic, respectively. The temperature profile in the lower electrode is linear in case of interfacial (blue and red solid lines) or null (green) electrochemical heat generation. However, in presence of the volumetric effect the profile becomes parabolic. As an example, the black dotted line shows the case where the electrochemical heat generation is released in the upper half part of the positive electrode ($\Delta h_{\mathrm{r}}/\Delta h_{\mathrm{P}} = 50\,\%$). As we see from Fig. 4c, we obtain always the strongest effect if we assume the electrochemical heat generation to be released at the interface (and not in the volume).

The electrochemical heat generation becomes more and more important when we reduce the current density, as already expected from Fig. 2a and shown in Fig. 4d. For the fully charged cell at $1\,\mathrm{A\,cm^{-2}}$ and in presence of electrochemical cooling, the temperature profile in the lower electrode has a negative slope. This may induce an unstable density stratification – and lead to convective flow if the Rayleigh number exceeds the critical value. More details, including the voltage at which the lower layer becomes isothermal, are presented in [60]. Finally, Fig. 4d shows also that the charging (or discharging of the battery) leads to a shift of the thermal peak due to the change of thickness of the liquid metal layers.

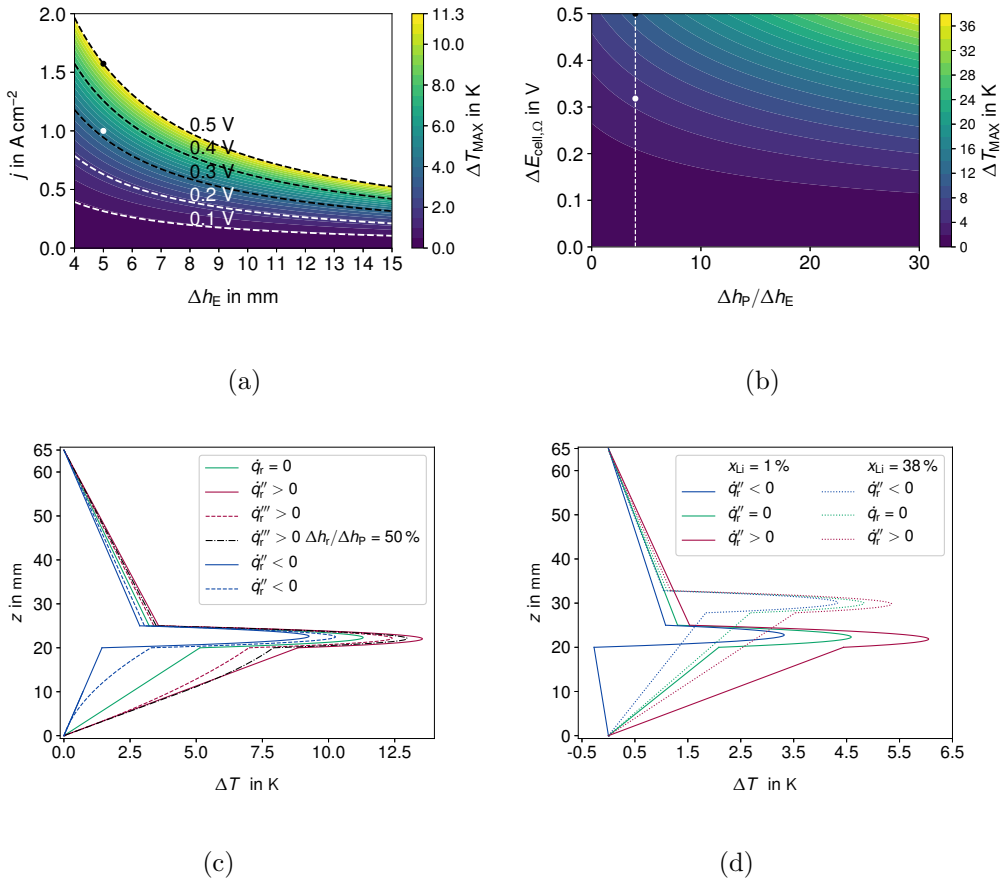

Figure 4: (a) Maximum cell temperature ($\Delta T_{\max} = T_{\max} - T_{\mathrm{b}}$) as function of the electrolyte thickness h_{E} and the current density j without electrochemical heat generation $\dot{q}_{\mathrm{r}}$. The white dot is the investigated case with the fully 3D simulation at $x_{\mathrm{Li}} = 1\,\%$. The black dot marks the maximum current density employed in the 1D study. (b) Maximum cell temperature $\Delta T_{\max}$ as function of $\Delta E_{\mathrm{cell},\Omega}$ and ratio between the layer thickness of positive electrode and electrolyte $\Delta h_{\mathrm{P}}/\Delta h_{\mathrm{E}}$, without electrochemical heat generation $\dot{q}_{\mathrm{r}}$. The white dashed line is for the geometry employed at $x_{\mathrm{Li}} = 1\,\%$. (c) Comparison between vertical temperature distributions in the presence and absence of volumetric ($\dot{q}_{\mathrm{r}}'''$ - dashed line) or interfacial ($\dot{q}_{\mathrm{r}}''$ - solid line) electrochemical heat generation. The maximum current density is $j_{\max} = 1.57\,\mathrm{A\,cm^{-2}}$, the electrolyte thickness $h_{\mathrm{E}} = 5\,\mathrm{mm}$. (d) Comparison between vertical temperature profiles in the presence and in absence of interfacial ($\dot{q}_{\mathrm{r}}''$) electrochemical heat generation at the selected current density $j = 1\,\mathrm{A\,cm^{-2}}$ for two different states of charge.

4.3. Thermo-fluid dynamic multiphase solver and discretization

In an LMB the transport of heat is not only governed by conduction (so far considered only), but also to a considerable extend by advection. In the following model, fluid flow is generated by thermally driven buoyancy forces, while we neglect Marangoni and MHD effects due to their supposedly smaller magnitude. Besides this source of momentum, momentum is transferred between the layers due to the mechanical coupling and by the interaction with the containment walls. The temperature dependence of the density of the fluids is described by a linear law ($\rho_i = \rho_{\mathrm{ref},i}(1 - \beta_i(T - T_{\mathrm{ref}}))$), in which $\rho_{\mathrm{ref},i}$ is the density of the i-th fluid calculated at the reference temperature T_{ref} of 450 °C and β_i is the volumetric thermal expansion coefficient. The density variations due to temperature changes are sufficiently small to assume an incompressible flow. The other properties are assumed to be constant with respect to the temperature.

At the walls we apply homogeneous Dirichlet boundary condition for both velocity components (no-slip and impermeable conditions). While previous studies [32, 33] used a multi-region approach, we employ a continuum field formulation with a homogeneous flow model [61] to study the fluid-dynamics of the cells. This is done in accordance to Weber et al. [23], in order to include MHD capabilities in a future development. The model is implemented in the finite volume (FVM) library OpenFOAM 4.0 [62] as an extension of the standard solver *multiphaseInterFoam*.

The incompressible Navier-Stokes equation (NSE) for a Newtonian fluid is reformulated in order to take into account the multiphase nature of the

system [63] as

$$\frac{\partial(\rho \boldsymbol{u})}{\partial t} + \nabla \cdot (\rho \boldsymbol{u}\boldsymbol{u}) = -\nabla p_{\mathrm{d}} + \mathrm{g} z \nabla \rho + \nabla \cdot (\rho \nu (\nabla \boldsymbol{u} + (\nabla \boldsymbol{u})^{\intercal})) + \boldsymbol{f}_{\mathrm{st}} \quad (11)$$

with ρ denoting density, $\boldsymbol{u}$ velocity, t time, g gravity acceleration, z the axial coordinate, ν kinematic viscosity and $\boldsymbol{f}_{\mathrm{st}}$ the source of momentum due to the surface tension. For the derivation of the modified pressure p_{d}, see [24, 63]. The interface capturing is done with the volume of fluid method (VOF), which uses a (volumetric) phase fraction α_i for each fluid i. The advection of these quantities [63, 64],

$$\frac{\partial \alpha_i}{\partial t} + \nabla \cdot (\alpha_i \boldsymbol{u}) = 0 \ , \quad (12)$$

together with the continuity equation $\nabla \cdot \boldsymbol{u} = 0$ guarantees the conservation of mass.

The surface tension is implemented (using the CSF model of Brackbill et al. [63–66]) as a volumetric force near the interface as $\boldsymbol{f}_{\mathrm{st}} = \sum_i \sum_{j \neq i} \gamma_{ij} \kappa_{ij} \delta_{ij}$ with γ_{ij} denoting the (constant) interface tension between the phases i and j. Concentration and temperature Marangoni effects are completely neglected. The curvature of the interface $i|j$ is

$$\kappa_{ij} = -\nabla \cdot \frac{\alpha_j \nabla \alpha_i - \alpha_i \nabla \alpha_j}{|\alpha_j \nabla \alpha_i - \alpha_i \nabla \alpha_j|}. \quad (13)$$

The term $\delta_{ij} = \alpha_j \nabla \alpha_i - \alpha_i \nabla \alpha_j$ applies the volumetric force only near the interfaces, where variations of the indicator function are present. Thus, the surface tension force becomes

$$\boldsymbol{f}_{\mathrm{st}} = -\sum_i \sum_{j \neq i} \gamma_{ij} \nabla \cdot \left(\frac{\alpha_j \nabla \alpha_i - \alpha_i \nabla \alpha_j}{|\alpha_j \nabla \alpha_i - \alpha_i \nabla \alpha_j|} \right) (\alpha_j \nabla \alpha_i - \alpha_i \nabla \alpha_j). \quad (14)$$

According with the hypotheses stated in section 4 the energy equation becomes:

$$c_p \left(\frac{\partial \rho T}{\partial t} + \nabla \cdot (\rho T \boldsymbol{u}) \right) = \nabla \cdot k \nabla T + \dot{q}'''_{\Omega} + \dot{q}'''_{\mathrm{r}}, \tag{15}$$

with c_p denoting the specific heat capacity. The two last terms represent the ohmic and the electrochemical heat generation, which were already specified in Eq. 7. Now we consider also the ohmic heat generation in the liquid metal layers, even if its effect is negligible. The electrochemical heat generation is implemented as a volumetric term $\dot{q}'''_{\mathrm{r}}$ which affects only a region of the lower layer of height Δh_{r}, just below the interface.

The thermodynamics and transport properties are computed in each computational cell using the volumetric phase fraction as a weighting factor as

$$\begin{gathered} \nu = \frac{1}{\rho} \sum_i \alpha_i \rho_i \nu_i \quad c_p = \frac{1}{\rho} \sum_i \alpha_i \rho_i c_{p,i} \quad k = \left(\sum_i \frac{\alpha_i}{k_i} \right)^{-1} \\ \rho_{\mathrm{el}} = \sum_i \alpha_i \rho_{\mathrm{el},i} \quad \text{and} \quad \rho = \sum_i \alpha_i \rho_{\mathrm{ref},i} (1 - \beta_i (T - T_{\mathrm{ref}})). \end{gathered} \tag{16}$$

The linear average is used for density and harmonic interpolation for the conductivities. Specific heat capacity and kinematic viscosity are linearly weighted by mass. For a detailed discussion of different blending schemes and their applicability, please refer to [64, 67–69]. Second order accurate schemes are used for time (backward scheme) and space discretization (linear scheme). The advection of temperature is discretized using the linearUpwind scheme while the bounded LUST scheme is used for velocity and vanLeer for the phase fractions [70]. The time step is determined using a Courant number of 0.5 based on the fluid velocity, interface displacement and capillary velocity; for more details see Appendix A.

4.4. Comparison with pseudo-spectral code

The OpenFOAM solver is validated by comparison with an established code [33] which uses a pseudo-spectral discretization. This reference solver was already successfully applied to a variety of solutal and thermal convection problems in two [71–74] and recently three-layer systems [33]. Its spatial discretization relies on the expansion of fields into Fourier modes for the x-y directions and Chebychev polynomials in the z direction. This type of discretization makes the code limited by means of geometry, namely only periodic boundary conditions on the side walls and non-deformable interfaces can be handled; but on the other hand, it features a high accuracy and small numerical costs. The recent developments of the code to capture three layers [33] have been validated by reproducing linear stability results, reproducing laminar flow, pure thermal conduction, as well as checking the kinetic energy balance.

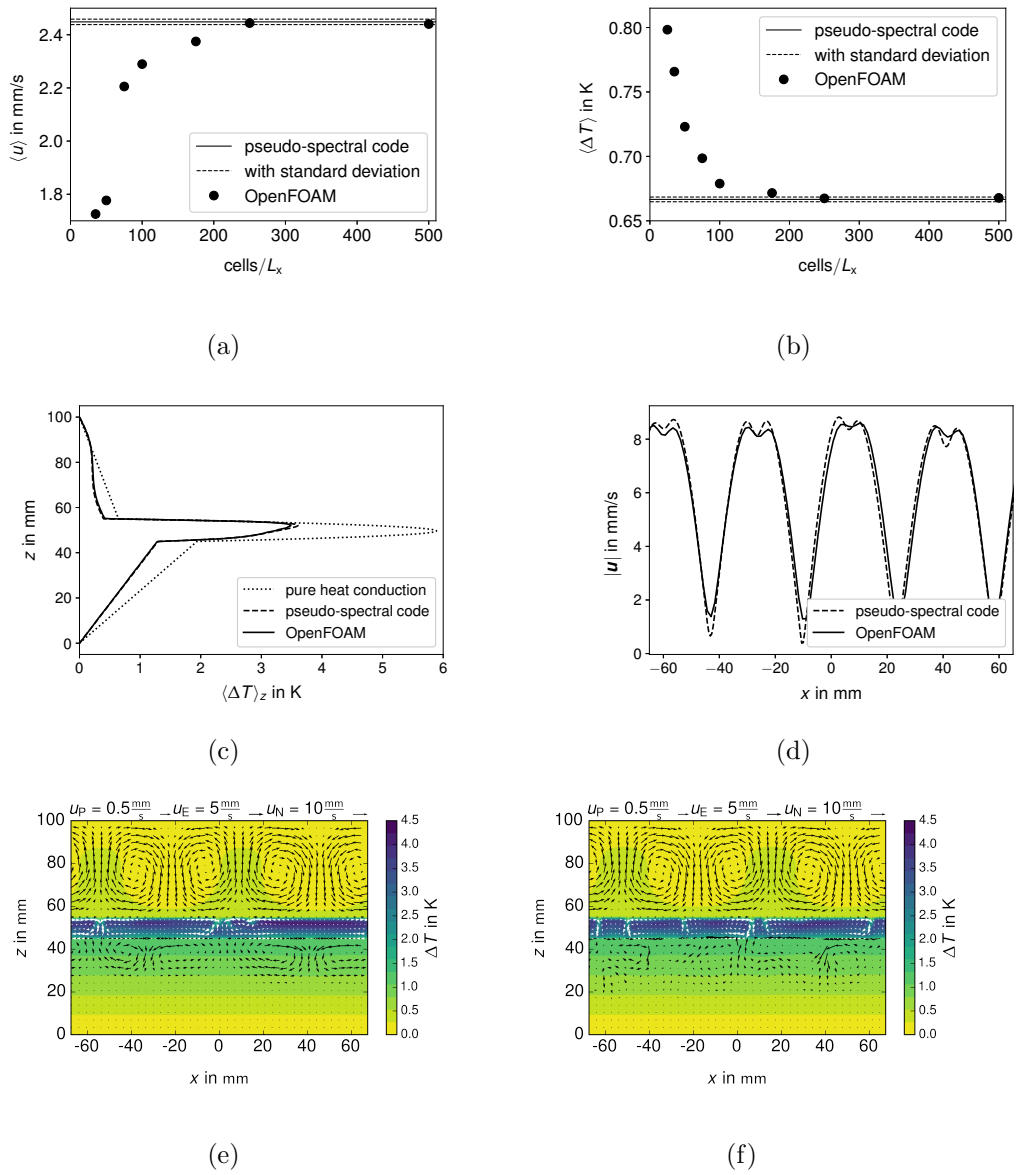

Figure 5: Grid study for volume averaged velocity (a) and volume averaged temperature (b), mean temperature profile along the vertical axis (c) and local velocity profile along a horizontal line (d) (at $z = 72.5\,\mathrm{mm}$) for the OpenFOAM solver and the spectral code. The general flow structure and temperature distribution of the pseudo-spectral (e) and the OpenFOAM solver (f). Note that we adapted the size of the velocity vectors for each phase with the reference values given in a legend above the subfigures.

The following 2D test case is used for comparison: The boundary condition at the side walls are assumed to be periodic, the temperature of top and bottom is set to 500 °C. The material properties of Köllner et al. [33] are employed. Furthermore, different dimensions ($L_\mathrm{x} = 135\,\mathrm{mm}$, $\Delta h_\mathrm{P} = \Delta h_\mathrm{N} = 45\,\mathrm{mm}$, $\Delta h_\mathrm{E} = 10\,\mathrm{mm}$) as shown in Fig. 5 are used, and the current density is set to $j = 0.5\,\mathrm{A\,cm^{-2}}$. A grid study yields converged results of velocity and temperature when using at least 250 cells ($N_\mathrm{x} = 250$) in the horizontal and 200 cells in the vertical direction ($N_\mathrm{z} = 200$). The mesh is strongly refined in the region of the electrolyte, near the interfaces and the wall.

For $N_x > 250$, the global mean velocity deviates less than 2 % and temperature by less than 1 % between the two solvers. The comparison is performed in thermal steady state condition; the profiles are time averaged over a period of 50 s, because the flow field is already in time-dependent, chaotic state. The horizontally averaged temperature in Fig. 5c and the local velocity magnitude in Fig. 5d (located in the middle of the light metal at $z = 72.5\,\mathrm{mm}$) agree very well with the reference pseudo-spectral solution. A snapshot of the velocity and temperature field is displayed for the pseudo-spectral code in Fig. 5e and for the OpenFOAM solver in (f) for qualitative comparison. The OpenFOAM solver captures especially well the flow structure and the temperature distribution in the top layer. Although the velocity magnitude in the two other layers is comparable between the two solvers, the flow structure shows some differences. This might have several reasons, as e.g. a less stable velocity distribution in the molten salt or the presence of spurious currents that affect the weak flow field in the lower layer.

Generally, a very good agreement was found between the OpenFOAM and pseudo-spectral code. This is a good result, because both approaches are very different. For further details about the grid study and the comparison, please refer to [60].

4.5. Results

The OpenFOAM solver is used to study the thermo-fluid dynamics of the cell in three states of charge (see section 3). We employ a current density of $1\,\mathrm{A\,cm^{-2}}$ and study both, the charge and discharge of the cell, with and without electrochemical heat generation. The latter is prescribed as a volumetric effect in the upper 10 % of the thickness of the positive electrode ($\Delta h_r = \frac{\Delta h_\mathrm{P}}{10}$).

The LMB domain is discretized with an unstructured orthogonal mesh. The latter is strongly refined in the electrolyte and near the walls in order to resolve local gradients, and near the interfaces in order to minimize numerical smearing. We employ 100 cells in horizontal and 75 cells in vertical direction with a total number of 7.5×10^5 cells.

The strongest fluid motion is observed in the top electrode, as shown in Fig. 6. The flow is driven by Rayleigh-Bénard convection, which is caused by a cold and rigid top wall, and a warm and deformable bottom surface (RB3 mode of [76]) in a laterally confined box. Due to the small aspect ratio and the square basis, the flow exhibits a fully 3D structure with symmetric features [77]. Although we did not find a critical Rayleigh number for the exact geometry and boundary conditions of the top layer, eight cases over nine exceed the value for a cubic cell ($Ra_\mathrm{cr} = 3389$) [77, 78] (see Fig. 7c). Fig. 6a shows the typical flow for the fully charged LMB: two counter ro-

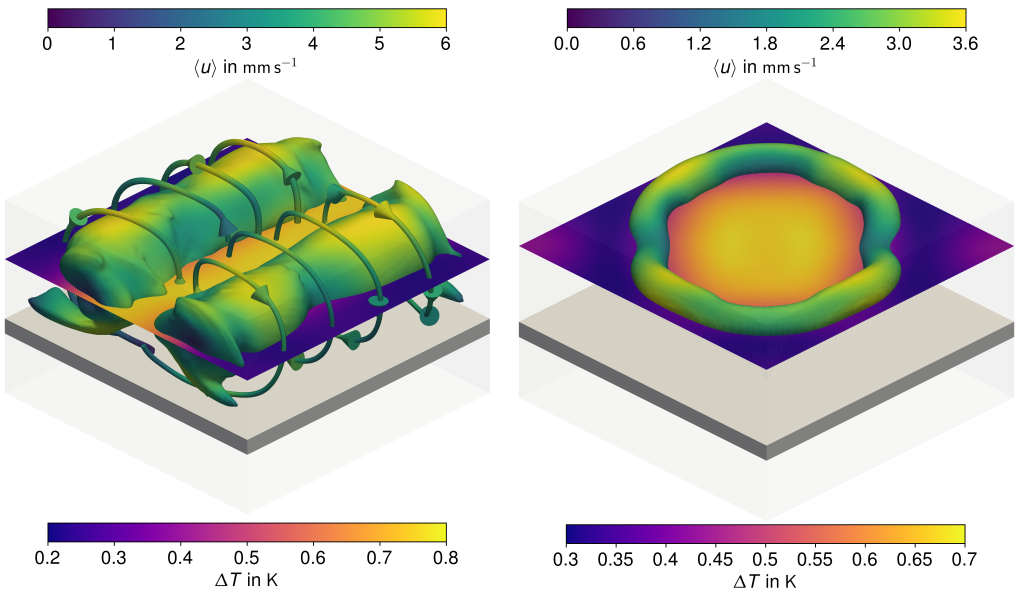

(a) (b)

Figure 6: Contours of the λ_2 criterion [75], flow velocity and temperature distribution in the negative electrode for the case at $x_{\mathrm{Li}} = 1\,\%$ showing two counter rotating vortices (a). Flow field and temperature distribution in the negative electrode for the case at $x_{\mathrm{Li}} = 38\,\%$ showing one vortex ring (b). The gray layer illustrates the electrolyte.

tating vortices can be observed in the negative electrode. During discharge the thickness of the top layer decreases and the aspect ratio increases from $AR_{\mathrm{N}} = \frac{L}{\Delta h_{\mathrm{N}}} = 2.5$ to $AR_{\mathrm{N}} = 3.14$. The flow structure completely changes and a stable vortex ring appears (Fig. 6b). The presence of a toroidal vortex is a known thermal convection mode in this configuration [79–81]. The fluid flow reduces the temperature of the side walls compared to pure conduction. The hot fluid rises in the central part of the cell and cools down before descending on lateral walls.

In all simulations performed by us, the electrolyte layer remains in a quies-

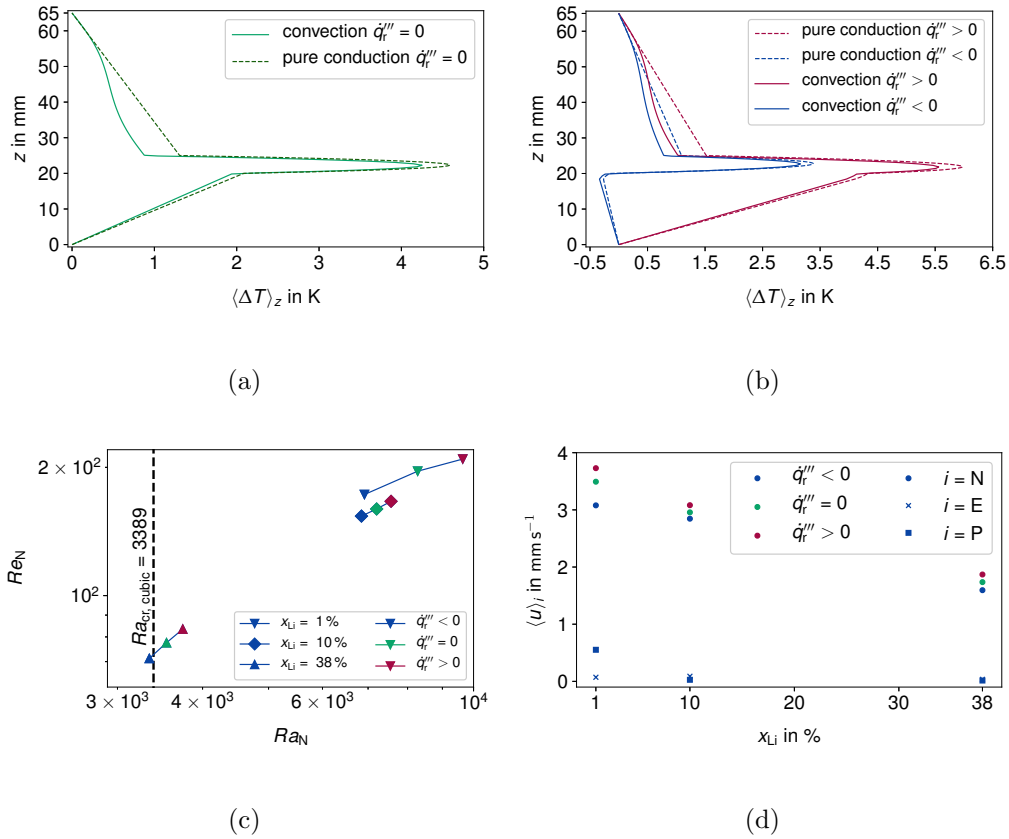

Figure 7: Three-dimensional simulation with the OpenFOAM solver: Mean temperature along the vertical axis without (a) and with electrochemical heat generation (b) for pure conduction and the convection case in the fully charged state. Reynolds ($Re_\mathrm{N} = \frac{\langle u \rangle_\mathrm{N} \Delta h_\mathrm{N}}{\nu_\mathrm{N}}$) and Rayleigh number ($Ra_\mathrm{N} = (\frac{\rho_\mathrm{ref} \cdot c_p \cdot \mathrm{g} \cdot \beta \cdot \Delta T_\mathrm{cd} \cdot \Delta h^3}{\nu \cdot k})_\mathrm{N}$) in the negative electrode with ΔT_cd denoting the conductive temperature difference (c). Volume averaged velocity in the three layers depending on the charge state with and without electrochemical heat generation (d). The current density is $j = 1\,\mathrm{A\,cm^{-2}}$.

cent state. The unstable density stratification is just too weak and affects a too small thickness (around 2.5 mm) to enhance and sustain a flow. Small velocity perturbations take place due to the viscous coupling with the nega-

tive electrode. The critical Rayleigh number for a layer subject to an internal heat generation and a temperature difference was derived by Sparrow et al. [82]. Assuming a laterally infinite layer, rigid walls and a non-linearity parameter $N_S = 3 \times 10^3$ we find a critical Rayleigh number of approximately $Ra_{\mathrm{cr}} = 583$. This value is exceeded in one single simulation ($Ra_{\mathrm{E}} = 671$), corresponding to a fully charged cell with positive electrochemical heat generation. Of course, convection will appear in a thicker electrolyte – as shown by previous studies [32, 33]. Nevertheless, the employment of thin electrolytes in the order of 5 mm is important to reduce ohmic losses.

The positive electrode is dominated by conduction. Only in one single case (fully charged cell and negative electrochemical heat generation) we obtain a temperature profile with an unstable density stratification. Although the Rayleigh number ($Ra_{\mathrm{P}} = (\frac{\rho_{\mathrm{ref}} \cdot c_p \cdot \mathrm{g} \cdot \beta \cdot \Delta T_{\mathrm{cd}} \cdot \Delta h^3}{\nu \cdot k})_{\mathrm{P}} = 1060$) is smaller than the critical one ($Ra_{\mathrm{cr}} = 1707$; infinite layer, no slip boundaries), we observe a weak flow.

Compared to pure conduction, the flow always reduces the observed temperature (Fig. 7a). This effect is especially strong in the negative electrode, where it lowers the maximum temperature up to 10 %. Anyway, the pure conduction model still provides a good approximation of the vertical temperature distribution.

The electrochemical heat generation affects the temperature profile in a very similar way as in pure conduction, as shown in Fig. 7b. While the flow structure does not change substantially, its magnitude does. Including the electrochemical heat generation into the model, the flow velocity changes up to 12 % in the negative electrode (Fig. 7d). As already expected [33], no

deformation of the interfaces was observed for all simulated cells.

5. Summary and outlook

In this paper we have discussed the thermal phenomena that take place in a liquid metal battery (LMB) using two different models. We have studied both: ohmic and electrochemical heat generation. The latter is taken into account for the first time together with thermal convection.

In a first step we developed an analytical 1D conduction model. It provides the vertical temperature distributions in the cell. This profile, derived from pure conduction, is the upper bound for the temperature and also the base state over which linear stability analysis can be performed. It can be used as an initial condition in thermo-fluid dynamic simulations. Furthermore, it allows to identify the region of the cell, which might be affected by convection and it is a good test model for the evaluation of the importance of different heat sources.

The electrochemical heat generation has an impact on the whole temperature profile. Most importantly, it is able to change the slope of the temperature profile in the bottom electrode, possibly leading to flow there. This very important as it could potentially enhance mass transfer. Compared to pure ohmic heating, the electrochemical heat is able to change the maximum cell temperature up to 30 %.

In a second step, we implemented a fully 3D thermo-fluid dynamic code that allows to study thermal convection inside the cell. For this purpose, the OpenFOAM Volume of Fluid solver was extended by a temperature dependent density and the energy equation. The arising problem of spurious

currents was addressed by implementing an additional time step limitation. Finally, the solver was validated by comparison with a pseudo-spectral code.

Thereafter, the solver was used to study a 10x10 cm Li||Bi square cell at three charge states. A mild flow in the order of mm/s was observed in the negative electrode. This flow was not able to deform the interfaces; therefore, we do not expect a short circuit of the battery to be induced by thermal convection. As our negative electrode consists of pure Li, the convection there does not affect the mass transport. However, we expect that the buoyancy driven flow can be relevant for mass transfer in multi-element LMBs which use an alloy as top electrode (e.g. Ca−Mg||Bi [83]).

Using a (realistic) electrolyte layer thickness of 5 mm and a high current density of $1\,\mathrm{A\,cm^{-2}}$, we found that the electrolyte is not subject to buoyancy driven flow. This is not in line with previous studies [32, 33], but can be explained by the thin electrolyte layer. Due to viscous coupling (and perhaps also spurious velocities), only a really weak flow in the order of 10 µm/s is induced in the electrolyte.

The stable density stratification in the positive electrode generally suppresses any fluid flow. However, it is possible that the electrochemical heat promotes convection in the lower electrode, and enhances mixing at the interface with the electrolyte. We observed that only in one single case.

Finally, we studied three different charge states of the cell. During discharge not only the location of the temperature peak will shift vertically – also the flow structure changes. While we observed two counter rotating vortices in the upper electrode of the fully charged cell, one vortex ring appears in the discharged cell at $x_{\mathrm{Li}} = 38\,\%$. We conclude that the charge state

strongly effects flow field and magnitude.

Our models are strongly simplified. Most importantly, an extended study of the electrochemical heat and especially its location should be performed. More detailed modeling should include radiative heat transfer (in the electrolyte and argon layer) and a mass transfer and solidification model. Finally, the boundary conditions will need improvement: e.g. the insulation and thermal management system may be included. Concerning the volume of fluid solver, more work should be dedicated to a solution of spurious velocities. The developed model can be applied in the future to other thermo and electro-metallurgical applications, as e.g. the study of titanium reduction reactors [84, 85].

Acknowledgments

This work was supported by Helmholtz-Gemeinschaft Deutscher Forschungszentren (HGF) in frame of the Helmholtz Alliance "Liquid metal technologies" (LIMTECH) as well as by the Deutsche Forschungsgemeinschaft (DFG, German Research Foundation) under award number 338560565 and grant number KO 5515/1-1. The computations were performed on the Bull HPC-Cluster "Taurus" at the Center for Information Services and High Performance Computing (ZIH) at TU Dresden, on the cluster "Hydra" at Helmholtz-Zentrum Dresden – Rossendorf and at the Computing Center of TU Ilmenau. Fruitful discussions with V. Galindo, D. Kelley, A. Teimurazov, V. Vukčević and O. Zikanov on several aspects of thermal convection and liquid metal batteries are gratefully acknowledged. N. Weber thanks H. Schulz for the HPC support.

References

[1] D. Lindley, Smart grids: The energy storage problem, Nature 463 (7277) (2010) 18–20.

[2] W. F. Pickard, Massive electricity storage for a developed economy of ten billion people, IEEE Access 3 (2015) 1392–1407.

[3] B. L. Spatocco, D. R. Sadoway, Cost-Based Discovery for Engineering Solutions, in: R. C. Alkire, P. N. Bartlett, J. Lipkowski (Eds.), Electrochemical Engineering Across Scales: From Molecules to Processes, Vol. 15 of Advances in Electrochemical Science and Engineering, Wiley-VCH, 2015, pp. 227–262.

[4] H. Kim, D. A. Boysen, J. M. Newhouse, B. L. Spatocco, B. Chung, P. J. Burke, D. J. Bradwell, K. Jiang, A. A. Tomaszowska, K. Wang, W. Wei, L. A. Ortiz, S. A. Barriga, S. M. Poizeau, D. R. Sadoway, Liquid Metal Batteries: Past, Present, and Future, Chem. Rev. 113 (3) (2013) 2075–2099. doi:10.1021/cr300205k.

[5] B. Agruss, Nuclear Liquid Metal Cell For Space Power, in: Proceedings of the 17th Power Sources Conference, 1963, pp. 100–103.

[6] E. J. Cairns, C. E. Crouthamel, A. K. Fischer, M. S. Foster, J. C. Hesson, C. E. Johnson, H. Shimotake, A. D. Tevebaugh, Galvanic Cells with Fused-Salt Electrolytes, ANL-7316, Argonne National Laboratory, 1967.

[7] E. J. Cairns, H. Shimotake, High-Temperature Batteries, Science 164 (1969) 1347–1355.

[8] H. Kim, D. A. Boysen, T. Ouchi, D. R. Sadoway, Calcium - bismuth electrodes for large - scale energy storage, J. Power Sources 241 (2013) 239–248.

[9] D. H. Kelley, T. Weier, Fluid mechanics of liquid metal batteries, Appl. Mech. Rev. 70 (2) (2018) 020801. doi:10.1115/1.4038699.

[10] X. Ning, S. Phadke, B. Chung, H. Yin, P. Burke, D. R. Sadoway, Self-healing Li–Bi liquid metal battery for grid-scale energy storage, J. Power Sources 275 (2015) 370–376. doi:10.1016/j.jpowsour.2014.10.173.

[11] F. Stefani, T. Weier, T. Gundrum, G. Gerbeth, How to circumvent the size limitation of liquid metal batteries due to the Tayler instability, Energy Convers. Manag. 52 (2011) 2982–2986. doi:10.1016/j.enconman.2011.03.003.

[12] N. Weber, V. Galindo, F. Stefani, T. Weier, T. Wondrak, Numerical simulation of the Tayler instability in liquid metals, New J. Phys. 15 (2013) 043034. doi:10.1088/1367-2630/15/4/043034.

[13] N. Weber, V. Galindo, F. Stefani, T. Weier, Current-driven flow instabilities in large-scale liquid metal batteries, and how to tame them, J. Power Sources 265 (2014) 166–173. doi:10.1016/j.jpowsour.2014.03.055.

[14] W. Herreman, C. Nore, L. Cappanera, J.-L. Guermond, Tayler instability in liquid metal columns and liquid metal batteries, J. Fluid Mech. 771 (2015) 79–114. doi:10.1017/jfm.2015.159.

[15] N. Weber, V. Galindo, F. Stefani, T. Weier, The Tayler instability at low magnetic Prandtl numbers: Between chiral symmetry breaking and helicity oscillations, New J. Phys. 17 (11) (2015) 113013. doi:10.1088/1367-2630/17/11/113013.

[16] T. Weier, A. Bund, W. El-Mofid, G. M. Horstmann, C.-C. Lalau, S. Landgraf, M. Nimtz, M. Starace, F. Stefani, N. Weber, Liquid metal batteries - materials selection and fluid dynamics, IOP Conf. Ser. Mater. Sci. Eng. 228 (2017) 012013. doi:10.1088/1757-899X/228/1/012013.

[17] D. Bradwell, G. Ceder, L. A. Ortiz, D. R. Sadoway, Liquid metal alloy energy storage device, US patent 9,076,996 B2 (2015).

[18] N. Weber, V. Galindo, J. Priede, F. Stefani, T. Weier, The influence of current collectors on Tayler instability and electro vortex flows in liquid metal batteries, Phys. Fluids 27 (2015) 014103. doi:10.1063/1.4905325.

[19] F. Stefani, V. Galindo, C. Kasprzyk, S. Landgraf, M. Seilmayer, M. Starace, N. Weber, T. Weier, Magnetohydrodynamic effects in liquid metal batteries, IOP Conf. Ser. Mater. Sci. Eng. 143 (2016) 012024. doi:10.1088/1757-899X/143/1/012024.

[20] R. Ashour, D. H. Kelley, A. Salas, M. Starace, N. Weber, T. Weier, Competing forces in liquid metal electrodes and batteries, J. Power Sources 378 (2018) 301–310. doi:10.1016/j.jpowsour.2017.12.042.

[21] N. Weber, M. Nimtz, P. Personnettaz, A. Salas, T. Weier, Electromagnetically driven convection suitable for mass transfer enhancement in liquid metal batteries, arXiv:1802.02214.

[22] O. Zikanov, Metal pad instabilities in liquid metal batteries, Phys. Rev. E 92 (2015) 063021.

[23] N. Weber, P. Beckstein, V. Galindo, W. Herreman, C. Nore, F. Stefani, T. Weier, Metal pad roll instability in liquid metal batteries, Magnetohydrodynamics 53 (1) (2017) 129–140.

[24] N. Weber, P. Beckstein, W. Herreman, G. M. Horstmann, C. Nore, F. Stefani, T. Weier, Sloshing instability and electrolyte layer rupture in liquid metal batteries, Phys. Fluids 29 (5) (2017) 054101. doi:10.1063/1.4982900.

[25] V. Bojarevics, A. Tucs, MHD of Large Scale Liquid Metal Batteries, in: A. P. Ratvik (Ed.), Light Metals 2017, Springer International Publishing, Cham, 2017, pp. 687–692.

[26] G. M. Horstmann, N. Weber, T. Weier, Coupling and stability of interfacial waves in liquid metal batteries, J. Fluid Mech. 845 (2018) 1–35. doi:10.1017/jfm.2018.223.

[27] O. Zikanov, Shallow water modeling of rolling pad instability in liquid metal batteries, arXiv:1706.08589.

[28] W. Wang, K. Wang, Simulation of thermal properties of the liquid metal batteries, in: 6th International Conference on Power Electronics Systems and Applications (PESA), IEEE, 2015, pp. 1–11.

[29] D. H. Kelley, D. R. Sadoway, Mixing in a liquid metal electrode, Phys. Fluids 26 (5) (2014) 057102. doi:10.1063/1.4875815.

[30] A. Perez, D. H. Kelley, Ultrasound Velocity Measurement in a Liquid Metal Electrode, J. Vis. Exp. 102 (2015) e52622. doi:10.3791/52622.

[31] A. Beltrán, MHD natural convection flow in a liquid metal electrode, Appl. Therm. Eng. 114 (2016) 1203–1212. doi:10.1016/j.applthermaleng.2016.09.006.

[32] Y. Shen, O. Zikanov, Thermal convection in a liquid metal battery, Theor. Comput. Fluid Dyn. 30 (4) (2016) 275–294. doi:10.1007/s00162-015-0378-1.

[33] T. Köllner, T. Boeck, J. Schumacher, Thermal Rayleigh-Marangoni convection in a three-layer liquid-metal-battery model, Phys. Rev. E 95 (2017) 053114. doi:10.1103/PhysRevE.95.053114.

[34] J. Newman, K. E. Thomas-Alyea, Electrochemical Systems, John Wiley & Sons, 2004.

[35] H. Heines, J. Westwater, The effect of heats of solution on marangoni convection, Int. J. Heat Mass Transf. 15 (11) (1972) 2109–2117. doi:10.1016/0017-9310(72)90035-X.

[36] K. Eckert, A. Grahn, Plume and finger regimes driven by an exothermic interfacial reaction, Phys. Rev. Lett. 82 (22) (1999) 4436.

[37] H. Grube, G. Vosskuehler, S. H., Elektrische Leitfähigkeit und

Zustandsdiagramm bei binären Legierungen. Das System Lithium-Wismuth., Z. Elektrochem. angew. p. 40 (5) (1934) 270–274.

[38] E. Zintl, G. Brauer, Metals and alloys. 14. constitution of Bi-Li alloys, Z. Elektochem. 41 (1935) 297–303.

[39] W. Seith, O. Kubaschewski, The heats of formation of several alloys, Z. Elektrochem. 43 (1937) 743–749.

[40] S. Shchukarev, M. Morozova, K. Yn, V. Sharov, Enthalpy of formation of Li and Ba bismuthides, Zh. Obshchei Khim 27(2) (1957) 290–93.

[41] M. Hansen, Constitution of Binary Alloys, McGraw-Hill, 1958.

[42] M. S. Foster, S. E. Wood, C. E. Crouthamel, Thermodynamics of Binary Alloys. I. The Lithium-Bismuth System, Inorg. Chem. 3 (10) (1964) 1428–1431.

[43] A. Demidov, A. G. Morachevskii, Thermodynamic properties of liquid lithium - bismuth alloys, Elektrokhimiya 9 (9) (1973) 1393–1394.

[44] M.-L. Saboungi, J. Marr, M. Blander, Thermodynamic properties of a quasi-ionic alloy from electromotive force measurements: The Li–Pb system, J. Chem. Phys. 68 (4) (1978) 1375. doi:10.1063/1.435957.

[45] B. Predel, G. Oehme, Calorimetric investigation of liquid Li–Tl, Li–In, and Li–Bi alloys, Z. Metallkd. 70 (9) (1979) 618–623.

[46] W. Gasior, Z. Moser, W. Zakulski, Bi-Li System. Thermodynamic properties and the phase diagram calculations, Arch. Metall. 39 (4) (1994) 355–364.

[47] J. Liu, J.-G. Zhang, Z. Yang, J. P. Lemmon, C. Imhoff, G. L. Graff, L. Li, J. Hu, C. Wang, J. Xiao, G. Xia, V. V. Viswanathan, S. Baskaran, V. Sprenkle, X. Li, Y. Shao, B. Schwenzer, Materials Science and Materials Chemistry for Large Scale Electrochemical Energy Storage: From Transportation to Electrical Grid, Adv. Funct. Mater. 23 (8) (2013) 929–946. doi:10.1002/adfm.201200690.

[48] Z. Cao, W. Xie, P. Chartrand, S. Wei, G. Du, Z. Qiao, Thermodynamic assessment of the Bi-alkali metal (Li, Na, K, Rb) systems using the modified quasichemical model for the liquid phase, Calphad 46 (2014) 159–167. doi:10.1016/j.calphad.2014.04.001.

[49] D. Bernardi, E. Pawlikowski, J. Newman, A general energy balance for battery systems, J. Electrochem. Soc. 132 (1) (1985) 5–12.

[50] J. Braunstein, G. Mamantov, G. P. Smith (Eds.), Advances in Molten Salt Chemistry, Springer US, Boston, MA, 1971.

[51] J. M. Newhouse, D. R. Sadoway, Charge-Transfer Kinetics of Alloying in Mg-Sb and Li-Bi Liquid Metal Electrodes, J. Electrochem. Soc. 164 (12) (2017) A2665–A2669.

[52] H. Shimotake, E. J. Cairns, Bimetallic galvanic cells with fused-salt electrolytes, in: Advances in Energy Conversion Engineering, ASME, Florida, 1967, pp. 951–962.

[53] H. L. Chum, R. A. Osteryoung, Review of Thermally Regenerative Electrochemical Cells, Solar Energy Research Institute, 1981.

[54] D. J. Bradwell, H. Nayar, Z. T. Modest, S. L. Golmon, Thermal management of liquid metal batteries, US patent US20160365612 A1 (2016).

[55] H. S. Carslaw, J. C. Jaeger, Conduction of Heat in Solids, Clarendon Press, 1959.

[56] W. B. Gu, C. Y. Wang, Thermal-electrochemical modeling of battery systems, J. Electrochem. Soc. 147 (8) (2000) 2910–2922.

[57] K. Kumaresan, G. Sikha, R. E. White, Thermal model for a Li-ion cell, J. Electrochem. Soc. 155 (2) (2008) A164–A171.

[58] J. K. Min, C.-H. Lee, Numerical study on the thermal management system of a molten sodium-sulfur battery module, J. Power Sources 210 (2012) 101–109.

[59] W. M. Deen, Analysis of Transport Phenomena, Topics in chemical engineering, Oxford University Press, New York, 1998.

[60] P. Personnettaz, Assessment of thermal phenomena in Li||Bi liquid metal batteries through analytical and numerical models, master thesis, Politecnico di Torino (2017).

[61] M. Wörner, A compact introduction to the numerical modeling of multiphase flows, Forschungszentrum Karlsruhe, 2003.

[62] H. G. Weller, G. Tabor, H. Jasak, C. Fureby, A tensorial approach to computational continuum mechanics using object-oriented techniques, Comput. Phys. 12 (6) (1998) 620–631.

[63] H. Rusche, Computational Fluid Dynamics of Dispersed Two-Phase Flows at High Phase Fractions, Ph.D. thesis, Imperial College London (2002).

[64] O. Ubbink, Numerical prediction of two fluid systems with sharp interfaces, Ph.D. thesis, University of London (1997).

[65] J. U. Brackbill, D. B. Kothe, C. Zemach, A continuum method for modeling surface tension, J. Comput. Phys. 100 (1992) 335–354.

[66] K. Kissling, J. Springer, H. Jasak, S. Schutz, K. Urban, M. Piesche, A coupled pressure based solution algorithm based on the volume-of-fluid approach for two or more immiscible fluids, in: Proceedings of the V European Conference on Computational Fluid Dynamics ECCOMAS CFD 2010, 2010, pp. 1–16.

[67] J. K. Carson, S. J. Lovatt, D. J. Tanner, A. C. Cleland, Thermal conductivity bounds for isotropic, porous materials, Int. J. Heat Mass Transf. 48 (11) (2005) 2150–2158. doi:10.1016/j.ijheatmasstransfer.2004.12.032.

[68] S. S. Kumar, Y. M. C. Delauré, Convective Heat Transfer of an Air Bubble in Water With Variable Thermophysical Properties, Heat Transf. Eng. 35 (14-15) (2014) 1370–1379. doi:10.1080/01457632.2013.877317.

[69] M. Nabil, A. S. Rattner, interThermalPhaseChangeFoam-A framework for two-phase flow simulations with thermally driven phase change, SoftwareX 5 (2016) 216–226. doi:10.1016/j.softx.2016.10.002.

[70] C. Greenshields, OpenFOAM User Guide (2016).

[71] T. Boeck, A. Nepomnyashchy, I. Simanovskii, A. Golovin, L. Braverman, A. Thess, Three-dimensional convection in a two-layer system with anomalous thermocapillary effect, Phys. Fluids 14 (11) (2002) 3899–3911. doi:10.1063/1.1506923.

[72] T. Boeck, M. Jurgk, U. Bahr, Oscillatory Rayleigh-Marangoni convection in a layer heated from above: Numerical simulations with an undeformable free surface, Phys. Rev. E 67 (2) (2003) 027303. doi:10.1103/PhysRevE.67.027303.

[73] T. Köllner, M. Rossi, F. Broer, T. Boeck, Chemical convection in the methylene-blue–glucose system: Optimal perturbations and three-dimensional simulations, Phys. Rev. E 90 (5) (2014) 053004. doi:10.1103/PhysRevE.90.053004.

[74] T. Köllner, K. Schwarzenberger, K. Eckert, T. Boeck, The eruptive regime of mass-transfer-driven Rayleigh–Marangoni convection, J. Fluid Mech. 791 (2016) R4. doi:10.1017/jfm.2016.63.

[75] J. Jeong, F. Hussain, On the identification of a vortex, Journal of fluid mechanics 285 (1995) 69–94.

[76] D. Goluskin, Internally Heated Convection and Rayleigh-Bénard Convection, Springer International Publishing, Cham, 2016. doi:10.1007/978-3-319-23941-5.

[77] M. Lappa, On the nature and structure of possible three-dimensional steady flows in closed and open parallelepipedic and cubical containers

under different heating conditions and driving forces, Fluid Mechanics and Material Processing 1 (2005) 1–19.

[78] D. Puigjaner, J. Herrero, F. Giralt, C. Simó, Stability analysis of the flow in a cubical cavity heated from below, Phys. Fluids 16 (10) (2004) 3639–3655.

[79] A. Y. Gelfgat, Different Modes of Rayleigh-Bénard Instability in Two- and Three-Dimensional Rectangular Enclosures, J Comput Phys 156 (1999) 300 – 324.

[80] J. Pallares, F. Grau, F. Giralt, Flow transitions in laminar rayleigh–bénard convection in a cubical cavity at moderate rayleigh numbers, International Journal of Heat and Mass Transfer 42 (4) (1999) 753–769.

[81] M. Funakoshi, Onset of thermal convection in a rectangular parallelepiped cavity of small aspect ratios, Fluid Dynamics Research 50 (2) (2018) 021402.

[82] E. Sparrow, R. Goldstein, V. Jonsson, Thermal instability in a horizontal fluid layer: effect of boundary conditions and non-linear temperature profile, J. Fluid Mech. 18 (4) (1964) 513–528.

[83] T. Ouchi, H. Kim, B. L. Spatocco, D. R. Sadoway, Calcium-based multi-element chemistry for grid-scale electrochemical energy storage, Nat. Commun. 7 (2016) 10999. doi:10.1038/ncomms10999.

[84] A. Teimurazov, P. Frick, F. Stefani, Thermal convection of liquid metal in the titanium reduction reactor, IOP Conf. Ser. Mater. Sci. Eng. 208 (2017) 012041. doi:10.1088/1757-899X/208/1/012041.

[85] A. Teimurazov, P. Frick, N. Weber, F. Stefani, Numerical simulations of convection in the titanium reduction reactor, J. Phys. Conf. Ser. 891 (2017) 012076. doi:10.1088/1742-6596/891/1/012076.

[86] A. Q. Raeini, M. J. Blunt, B. Bijeljic, Modelling two-phase flow in porous media at the pore scale using the volume-of-fluid method, J. Comput. Phys. 231 (17) (2012) 5653–5668. doi:10.1016/j.jcp.2012.04.011.

[87] D. Harvie, M. Davidson, M. Rudman, An analysis of parasitic current generation in Volume of Fluid simulations, Appl. Math. Model. 30 (10) (2006) 1056–1066. doi:10.1016/j.apm.2005.08.015.

[88] T. Abadie, J. Aubin, D. Legendre, On the combined effects of surface tension force calculation and interface advection on spurious currents within Volume of Fluid and Level Set frameworks, J. Comput. Phys. 297 (2015) 611–636. doi:10.1016/j.jcp.2015.04.054.

[89] V. Vukcevic, Numerical modelling of coupled potential and viscous flow for marine applications, Ph.D. thesis, University of Zagreb, Zagreb (2016).

[90] V. Vukčević, H. Jasak, I. Gatin, Implementation of the Ghost Fluid Method for free surface flows in polyhedral Finite Volume framework, Comput. Fluids 153 (2017) 1–19. doi:10.1016/j.compfluid.2017.05.003.

[91] J. Huang, P. M. Carrica, F. Stern, Coupled ghost fluid/two-phase level

set method for curvilinear body-fitted grids, Int. J. Numer. Methods Fluids 55 (9) (2007) 867–897. doi:10.1002/fld.1499.

[92] D. A. Hoang, V. van Steijn, L. M. Portela, M. T. Kreutzer, C. R. Kleijn, Benchmark numerical simulations of segmented two-phase flows in microchannels using the Volume of Fluid method, Comput. Fluids 86 (2013) 28–36.

[93] S. Popinet, An accurate adaptive solver for surface-tension-driven interfacial flows, J. Comput. Phys. 228 (16) (2009) 5838–5866. doi:10.1016/j.jcp.2009.04.042.

[94] M. M. Francois, S. J. Cummins, E. D. Dendy, D. B. Kothe, J. M. Sicilian, M. W. Williams, A balanced-force algorithm for continuous and sharp interfacial surface tension models within a volume tracking framework, J. Comput. Phys. 213 (2006) 141–173.

[95] C. B. Ivey, P. Moin, Accurate interface normal and curvature estimates on three-dimensional unstructured non-convex polyhedral meshes, J. Comput. Phys. 300 (2015) 365–386. doi:10.1016/j.jcp.2015.07.055.

[96] A. Albadawi, D. Donoghue, A. Robinson, D. Murray, Y. Delauré, Influence of surface tension implementation in Volume of Fluid and coupled Volume of Fluid with Level Set methods for bubble growth and detachment, Int. J. Multiph. Flow 53 (2013) 11–28. doi:10.1016/j.ijmultiphaseflow.2013.01.005.

[97] T. Yamamoto, Y. Okano, S. Dost, Validation of the S-CLSVOF method with the density-scaled balanced continuum surface force model in multiphase systems coupled with thermocapillary flows, Int. J. Numer. Methods Fluids 83 (3) (2016) 223–244. doi:10.1002/fld.4267.

[98] M. Dianat, M. Skarysz, A. Garmory, A Coupled Level Set and Volume of Fluid method for automotive exterior water management applications, Int. J. Multiph. Flow 91 (2017) 19–38. doi:10.1016/j.ijmultiphaseflow.2017.01.008.

[99] M. Haghshenas, J. A. Wilson, R. Kumar, Algebraic coupled level set-volume of fluid method for surface tension dominant two-phase flows, Int. J. Multiph. Flow 90 (2017) 13–28. doi:10.1016/j.ijmultiphaseflow.2016.12.002.

[100] C. Galusinski, P. Vigneaux, On stability condition for bifluid flows with surface tension: Application to microfluidics, J. Comput. Phys. 227 (12) (2008) 6140–6164. doi:10.1016/j.jcp.2008.02.023.

[101] F. Denner, B. G. van Wachem, Numerical time-step restrictions as a result of capillary waves, J. Comput. Phys. 285 (2015) 24–40. doi:10.1016/j.jcp.2015.01.021.

[102] S. J. Zinkle, Summary of Physical Properties for Lithium, Pb-17Li, and (LiF)n•BeF2 Coolants, in: APEX Study Meeting, 1998, pp. 1 – 8.

[103] C. Fazio, V. Sobolev, A. Aerts, S. Gavrilov, K. Lambrinou, P. Schuurmans, A. Gessi, P. Agostini, A. Ciampichetti, L. Martinelli, et al., Handbook on lead-bismuth eutectic alloy and lead properties, materials

compatibility, thermal-hydraulics and technologies., Tech. Rep. 7268, Organisation for Economic Co-Operation and Development (2015).

[104] C. J. Raseman, H. Susskind, G. Farber, W. McNulty, F. Salzano, Engineering experience at Brookhaven National Laboratory in handling fused chloride salts, Tech. Rep. BNL 627, Brookhaven National Laboratory (1960).

[105] G. J. Janz, C. B. Allen, N. P. Bansal, R. M. Murphy, R. P. T. Tomkins, Physical Properties Data Compilations Relevant to Energy Storage. II. Molten Salts: Data on Single and Multi-Component Salt Systems, U. S. Department of Commerce, 1979.

[106] G. J. Janz, Thermodynamic and Transport Properties for Molten Salts: Correlation Equations for Critically Evaluated Density, Surface Tension, Electrical Conductance, and Viscosity Data, no. 17 in J. Phys. Chem. Ref. Data, American Chemical Society and the American Institute of Physics, 1988.

[107] L. A. Girifalco, R. J. Good, A theory for the estimation of surface and interfacial energies. I. Derivation and application to interfacial tension, J. Phys. Chem. 61 (7) (1957) 904–909.

[108] R. J. Good, E. Elbing, Generalization of theory for estimation of interfacial energies, Ind. Eng. Chem. 62 (3) (1970) 54–78.

[109] N. Shaikhmahmud, Interfacial Tensions of Molten Metal-Molten Salt Systems : Bismuth against KCl-LiCl Eutectic Mixture / by N.S.

Shaikhmahmud, C.F. Bonilla., United States Atomic Energy Commission, New York, 1953.

[110] R. R. Roy, T. A. Utigard, Interfacial tension between aluminum and NaCl-KCl-based salt systems, Metall. Mater. Trans. B 29 (4) (1998) 821–827.

[111] R. Roy, Y. Sahai, Interfacial tension between Aluminium Alloy and Molten Salt Flux, Mater. Trans. 38 (6) (1997) 546–552.

[112] W. Gasior, Viscosity modeling of binary alloys: Comparative studies, Calphad 44 (2014) 119–128.

[113] K. Cornwell, The thermal conductivity of molten salts, J. Phys. Appl. Phys. 4 (3) (1971) 441.

Appendix A. Spurious velocities

Spurious currents are unphysical velocities well known in volume of fluid (VOF) simulations [86–88]. One source of such artificial flows is an imbalance between the pressure and density gradient (eqn. 11) due to the continuous interpolation of density (or viscosity) [89, 90]. This type of parasitic currents is strong for large density jumps and appears predominantly in the lighter phase [91]. A second type of spurious currents is caused by the imbalance between the surface tension force (Eq. 14) and pressure gradient [92, 93] due to a poor calculation of the interface curvature (Eq. 13) [92, 94]. Moreover, this surface tension term may contain an erroneous rotational component that cannot be balanced by the irrotational pressure term [87]. This will be an additional source of spurious currents. Finally, also the interface compression term in the phase transport equation [63] could lead to some unphysical currents.

Naturally, all spurious currents can be reduced by lowering the pressure residual. Type one spurious velocities may be eliminated by an exact discretization of the pressure jump, i.e. by using the idea of the ghost fluid method [90, 91]. Interface tension related erroneous flows are best treated by improving the curvature calculation. This might be done using an (additional) height or level set function [92, 95–99]. Furthermore, a posterior damping of spurious velocities is possible by smoothing the curvature field and filtering interface-parallel velocities [86].

Finally, the interface tension γ is discretized explicitly when using the CSF model [65]. Therefore, the capillary number must be respected as an

additional time step constraint [100, 101]:

$$\Delta t = \sqrt{\frac{(\rho_A + \rho_B)\Delta x^3}{2\pi\gamma_{\max}}} \cdot \mathrm{Co}_{\mathrm{cap}}. \tag{A.1}$$

Here, ρ_A and ρ_B denote the two smallest densities, Δx^3 the cell volume, $\gamma_{\max}$ the largest interface tension and $\mathrm{Co}_{\mathrm{cap}}$ the capillary Courant number.

Implementing this time step restriction (for $\mathrm{Co}_{\mathrm{cap}} = 0.5$), removing the artificial interface compression and reducing the pressure residual to 10^{-8} we were able to reduce spurious velocities from $1\,\mathrm{cm\,s^{-1}}$ to $30\,\mu\mathrm{m\,s^{-1}}$ in our setup.

Appendix B. Constants for heat conduction model

$$c_1 = \frac{(\dot{q}''_{\mathrm{r}} + \dot{q}'''_{\mathrm{r}}(h_{\mathrm{P}} - h_0) - \dot{q}'''_{\Omega} h_{\mathrm{P}})}{k_{\mathrm{P}}} + \frac{k_{\mathrm{E}}}{k_{\mathrm{P}}} c_5$$

$$c_2 = T_{\mathrm{b}}$$

$$c_3 = \frac{(\dot{q}'''_{\mathrm{r}} - \dot{q}'''_{\Omega}) h_{\mathrm{P}} + \dot{q}''_{\mathrm{r}}}{k_{\mathrm{P}}} + \frac{k_{\mathrm{E}}}{k_{\mathrm{P}}} c_5$$

$$c_4 = T_{\mathrm{b}} - \frac{\dot{q}'''_{\mathrm{r}} h_{\mathrm{r}}^2}{2k_{\mathrm{P}}}$$

$$c_5 = \frac{\dot{q}'''_{\Omega,\mathrm{E}}(2k_{\mathrm{P}}k_{\mathrm{E}}\left(h_{\mathrm{E}}h_{\mathrm{N}} - h_{\mathrm{E}}^2\right) + k_{\mathrm{P}}k_{\mathrm{N}}\left(h_{\mathrm{E}}^2 - h_{\mathrm{P}}^2\right)) + k_{\mathrm{E}}k_{\mathrm{N}}\left(\dot{q}'''_{\mathrm{r}} h_{\mathrm{r}}^2 - 2\dot{q}''_{\mathrm{r}} h_{\mathrm{P}} + h_{\mathrm{P}}^2\left(2\dot{q}'''_{\Omega} - \dot{q}'''_{\mathrm{r}}\right)\right)}{2k_{\mathrm{E}}\left(h_{\mathrm{P}}k_{\mathrm{E}}k_{\mathrm{N}} - h_{\mathrm{P}}k_{\mathrm{P}}k_{\mathrm{N}} - h_{\mathrm{E}}k_{\mathrm{P}}k_{\mathrm{E}} + h_{\mathrm{E}}k_{\mathrm{P}}k_{\mathrm{N}} + h_{\mathrm{N}}k_{\mathrm{P}}k_{\mathrm{E}}\right)}$$

$$c_6 = T_{\mathrm{b}} + h_{\mathrm{P}} c_5 (\frac{k_{\mathrm{E}}}{k_{\mathrm{P}}} - 1) + \frac{\dot{q}'''_{\mathrm{r}}(h_{\mathrm{P}}^2 - h_{\mathrm{r}}^2) + 2h_{\mathrm{P}}(\dot{q}''_{\mathrm{r}} - \dot{q}'''_{\Omega} h_{\mathrm{P}})}{2k_{\mathrm{P}}} + \frac{\dot{q}'''_{\Omega} h_{\mathrm{P}}^2}{2k_{\mathrm{E}}}$$

$$c_7 = \frac{k_{\mathrm{E}}}{k_{\mathrm{N}}} (c_5 - \frac{\dot{q}'''_{\Omega} h_{\mathrm{E}}}{k_{\mathrm{E}}})$$

$$c_8 = T_{\mathrm{b}} - h_{\mathrm{N}} c_7$$

Appendix C. Material properties and layer height

In this appendix the thermo-physical and transport properties are collected.

The material properties of Li are taken from Zinkle et al. [102], and for Bi by Fazio et al. [103]. Specific heat capacity and viscosity of the molten salt mixture (KCl−LiCl) are evaluated with the formulation suggested by Raseman et al. [104], for the other properties the values given by Janz are used [105, 106]. All thermo-physical and transport properties of the pure materials of the cell are evaluated at 450 °C and summarized in Tab. C.2.

The interface tensions can be approximated from the surface tensions of the pure substances, using the rule proposed by Girifalco and Good [107, 108]:

$$\gamma = \gamma_i + \gamma_j - 2\phi\sqrt{\gamma_i \gamma_j}. \tag{C.1}$$

The interaction parameter ϕ for Bi|KCl−LiCl is given by Shaikhmahmud et al. [109] as $\phi = 0.58$. No information is available for the couple Li|KCl−LiCl. However, the values for similar material combinations (e.g. 0.41 for Al|cryolite [110], 0.51 for Al|NaCl-KCl [111]) suggest that assuming $\phi = 0.5$ is reasonable. Using $\phi = 0.5$ we obtain an interface tension of $\gamma = 0.196\,\mathrm{N\,m^{-1}}$ for Li|KCl−LiCl and $\gamma = 0.275\,\mathrm{N\,m^{-1}}$ for KCl−LiCl|Bi.

The material properties of the Bi−Li alloy in the concentration range of interest are not available in literature. We assume a pure bismuth positive electrode in full charge condition ($x_{\mathrm{Li}} = 1\,\%$). For higher concentration of Li the values are approximated from the properties of the pure components. The mixture densities are calculated by the Vegard's law using the mole fraction [103]. These values are used to calculate the positive electrode thickness. The

specific heat capacity of the Bi−Li alloy is calculated by Neumann-Kopp's law with the mass fraction. The surface tension of Bi−Li alloy is assumed to be equal to the one of pure bismuth. The viscosity of the mixture is calculated with a simple linear interpolation using the mole fractions, without taking into account the correction based on the thermodynamic potential proposed by Gasior et al. [112]. Regarding electrical and thermal conductivity, the values of pure bismuth are employed also for the alloy. In Tab. C.3 the dimensions of the cell at different charge states as well as the material properties of the mixture Bi−Li are provided.

Table C.2: Thermo-physical and transport properties of the pure substances at $T = 450\,°\mathrm{C}$ [102–106, 113].

property	unit	Li	LiCl-KCl	Bi
ρ_{ref}	$\mathrm{kg\,m^{-3}}$	491.3	1648	9843
β	$10^{-4}\,\mathrm{K^{-1}}$	1.80	3.20	1.24
c_p	$\mathrm{J\,kg^{-1}\,K^{-1}}$	4237	1330	136
γ	$\mathrm{Nm^{-1}}$	0.292	0.130	0.362
ν	$10^{-7}\,\mathrm{m^2\,s^{-1}}$	7.13	19.8	1.33
ρ_{el}	$10^{-6}\,\Omega\,\mathrm{m}$	0.367	6358	1.39
k	$\mathrm{W\,m^{-1}\,K^{-1}}$	51.9	0.69	14.2

Table C.3: Mole fractions of lithium in bismuth, layer heights and Bi−Li mixture properties (of the positive electrode) at different charge states [102, 103].

property	unit	cases studied		
x_{Li}	%	1	10	38
Δh_{P}	mm	20	21.3	27.8
Δh_{E}	mm	5	5	5
Δh_{N}	mm	40	38.5	31.8
ρ_{ref}	$\mathrm{kg\,m^{-3}}$	9843	9238	7222
β	$10^{-4}\,\mathrm{K^{-1}}$	1.24	1.30	1.48
c_p	$\mathrm{J\,kg^{-1}\,K^{-1}}$	136	151.3	218.0
γ	$\mathrm{Nm^{-1}}$	0.362	0.362	0.362
ν	$10^{-7}\,\mathrm{m^2\,s^{-1}}$	1.33	1.31	1.31
ρ_{el}	$10^{-6}\,\Omega\,\mathrm{m}$	1.39	1.39	1.39
k	$\mathrm{W\,m^{-1}\,K^{-1}}$	14.2	14.2	14.2